CARBON ENERGY Open Access

WILEY

Unassisted Photoelectrochemical CO_2 Reduction by Employing III-V Photoelectrode with 15% Solar-to-Fuel Efficiency

Karthik Peramaiah,[#] Purushothaman Varadhan,[#] Vinoth Ramalingam,[#] Bilawal Khan, Pradip Kumar Das, Hao Huang, Hui-Chun Fu, Xiulin Yang, Vincent Tung, Kuo-Wei Huang[*] and Jr-Hau He[*]*

Dr. Karthik Peramaiah, Dr. Purushothaman Varadhan, Dr. Vinoth Ramalingam, Dr. Hao Huang, Dr. Hui-Chun Fu, Prof. Kuo-Wei Huang, Prof. Jr-Hau He

KAUST Catalysis Center and Division of Physical Science and Engineering, King Abdullah University of Science and Technology, Thuwal, 23955-6900, Saudi Arabia.

Dr. Karthik Peramaiah, Prof. Kuo-Wei Huang, Dr. Pradip Kumar Das

Institute of Sustainability for Chemicals, Energy, and Environment ($ISCE^2$), Agency for Science, Technology and Research (A*STAR), 1 Pesek Road, 627833, Singapore.

Dr. Vinoth Ramalingam

School of Engineering, Robert Gordon University, Garthdee Road, Aberdeen AB10 7GJ, United Kingdom.

Bilawal Khan

Department of Materials Science and Engineering, City University of Hong Kong, Kowloon, SAR 999077 Hong Kong.

Dr. Xiulin Yang

Guangxi Key Laboratory of Low Carbon Energy Materials, School of Chemistry and Pharmaceutical Sciences, Guangxi Normal University, Guilin 541004, China.

Prof. Vincent Tung

Department of Chemical System and Engineering, University of Tokyo, Tokyo, Japan.

Prof. Jr-Hau He

Department of Materials Science and Engineering, City University of Hong Kong, Kowloon, SAR 999077 Hong Kong

[#]equally contributed

Keywords: unassisted PEC, CO_2 reduction, 3J photoanode, high STF.

[*]Corresponding authors: karthik.peramaiya@kaust.edu.sa; hkw@kaust.edu.sa; jrhauhe@cityu.edu.hk

CARBON ENERGY Open Access

WILEY

ABSTRACT

Solar-driven CO_2 reduction reaction (CO_2RR) provides an opportunity to produce value-added chemical feedstocks and fuels. However, achieving efficient and stable photoelectrochemical (PEC) CO_2RR into selective products is challenging owing to the difficulties associated with the optical and electrical configuration of PEC devices and electrocatalyst properties. Herein, we construct an efficient, concentrated sunlight-driven CO_2RR setup consisting of InGaP/GaAs/Ge triple-junction cell (TJ) as a photoanode and oxide-derived Au (Ox-Au) as a cathode to perform the unassisted CO_2RR. Under one-sun illumination, a maximum operating current density of 11.5 mA cm^{-2} with an impressive Faradaic efficiency (FE) of ~98% is achieved for CO production, leading to a solar-to-fuel (STF) conversion efficiency of ~15%. Under concentrated intensity of 10 sun, the photoanode recorded a current density of ~124 mA cm^{-2} and maintained ~60% of FE for CO production. The results demonstrate crucial advancements in using III-V photoanodes for concentrated PEC CO_2 reduction.

1. Introduction

Solar-powered CO_2 reduction reaction (CO_2RR) is one of the promising methods to convert CO_2 into value-added chemicals and fuels using renewable solar energy[1–5]. In comparison to other energy conversion approaches, such as photocatalytic (PC) and electrocatalytic (EC), the photoelectrochemical (PEC) approach has gained significant attention due to the combined advantages of EC and PC processes. The PEC approach combines a light-harvesting system and electrochemical components into a single device. This approach has gained considerable attention for CO_2RR[6–10] and various other PEC applications, such as water splitting and nitrogen reduction reactions.[11–13] Among the wide range of CO_2 reduction products, carbon monoxide (CO) is a viable product due to its extensive applications in various industrial processes. Additionally, CO formation requires only two proton-electron transfer reactions, making it a kinetically favorable choice compared to other products such as CH_3OH, C_2H_4, and C_2H_5OH, etc, which require more than two proton-electron transfers to form.[5,14–16] Intensive efforts are underway to produce cost-competitive CO and syngas ($CO + H_2$) through an electrochemical approach for the industrial Fischer–Tropsch process.[8,17,18] Besides, designing and developing an efficient PEC CO_2RR system can also lead to the cost-competitive production of CO and syngas. In addition, different ratios of syngas mixtures can also be produced in the PEC approach due to the competitive H_2 evolution reaction.[19–21]

To design an efficient solar-driven system to reduce CO_2 into specific products, highly selective electrocatalysts are necessary to facilitate the CO_2RR preferentially at low overpotential[22,23]. Metals including Au, Ag, Cu, and Sn have been widely used as the catalyst for CO_2RR to achieve selective products in an aqueous electrolyte[24,25]. The catalytic activity of metals can be significantly improved through precise control of crystal facets, grain

boundaries, nano- and mesostructures, as well as oxidation states [26–29]. In particular, electrochemical anodization of metal is found to be helpful in achieving highly selective end-products by having controlled oxidation states of the catalysts with a porous surface.[28,29] Furthermore, anodized metal catalysts can have different shapes and grain boundaries, which can improve catalytic performance at low potential. In our study, we employed the pulsed anodization strategy to prepare the oxide-derived Au (Ox-Au) electrocatalyst and used it as the cathode. This significantly reduced the CO_2RR onset potential compared to bare Au foil and demonstrated an unassisted photoelectrochemical approach.

Various semiconductor photoelectrodes, including Si and III-V, have been investigated for solar-driven CO_2 reduction into CO, usually in conjunction with metal catalysts for selective reduction (e.g., Au, Ag, and derivatives). However, designing a PEC CO_2RR system with self-solar powered or unassisted configurations for redox couple reactions could be a promising approach as it reduces the resistive losses due to the external wiring between electrocatalytic parts and solar-powered devices[30,31]. An unassisted PEC system with a two-electrode configuration, in which photoelectrodes are attached with redox reaction catalysts, facilitates long-term effective solar-energy utilization at a low cost. However, it is still challenging to develop an efficient and stable unassisted PEC CO_2RR system due to the difficulty in the prerequisite of sufficiently high photovoltage-producing semiconductor system as most of the electrocatalysts have higher overpotential than hydrogen evolution reaction catalysts[32]. To build an unassisted CO_2RR system, tandem III-V photoelectrodes are commonly used.[33,34] While tandem III-V photoelectrodes can generate the required photovoltage for an unassisted PEC approach, their instability in aqueous electrolytes poses a significant challenge for long-term stability. The low stability of the photoelectrode is due to photocorrosion and chemical

instability in aqueous electrolytes, which needs to be prevented using suitable protection layers. In addition, using III-V semiconductors as a photoelectrode under one-sun intensity is not practically viable for solar fuel production as they cannot reach the industrial-level current density. Thus, addressing these challenges necessitates establishing a photoabsorber with optimal photovoltage, long-term stability, and a low-onset potential catalyst for a promising self-sustained PEC CO_2RR.

In this study, III-V-based triple-junction (TJ) InGaP/GaAs/Ge is employed for unassisted CO_2RR using an Ox-Au as a cathode catalyst. To enable the unassisted CO_2RR at low applied potential, we integrated RuO_x-deposited thin Ti-foil with the InGaP/GaAs/Ge triple junction cell, which served as the photoanode. This integrated system exhibited significant stability under aqueous electrolytes by preventing direct InGaP/GaAs/Ge contact with the electrolytes. Moreover, the two-electrode unassisted system achieved a ~98% Faradaic efficiency for CO production and an impressive solar-to-fuel (STF) efficiency of 15%. Notably, we demonstrated a more practical application of the III-V photoanode system by using concentrated sunlight to drive CO_2RR, resulting in a current density of ~124 mA/cm^2 without external bias.

2. Results and Discussion

2. 1. Anodized Au electrocatalyst

Oxide-derived Au (Ox-Au) porous structure with excellent CO_2RR catalytic performance was achieved by an electrochemical pretreatment method[29,35]. The pretreatment includes vigorous pulsed anodization followed by gentle reduction, which develops Ox-Au porous structures on the surface of a 3×3 cm^2 Au foil.[229] Pulsed anodization was initially employed to generate Au oxide on a thin Au film, applying potentials ranging from 1.2 V to 2.7 V versus a reversible hydrogen electrode (RHE) in a $KHCO_3$ solution (0.5 M, pH = 7.2). This process was conducted in a two-

compartment cell using a three-electrode configuration **(Figure 1a)**, where Pt, Ag/AgCl, and Au foil served as the counter, reference, and working electrodes, respectively. The two-compartment cell was separated by a Bipolar membrane B(PM) to minimize the deposition of impurities during the anodization process. Following pulsed anodization, we subsequently electrochemically reduced the anodic Au_2O_3 layer in the same electrolyte under a constant current density ranging from -0.1 to -0.5 mA cm^{-2} until the electrode potential stabilized **(Figure 1b)**. Post-treatment, the gold color of the Au thin film transformed to a dark brown hue, indicative of the formation of Au nanostructures on its surface.[35]

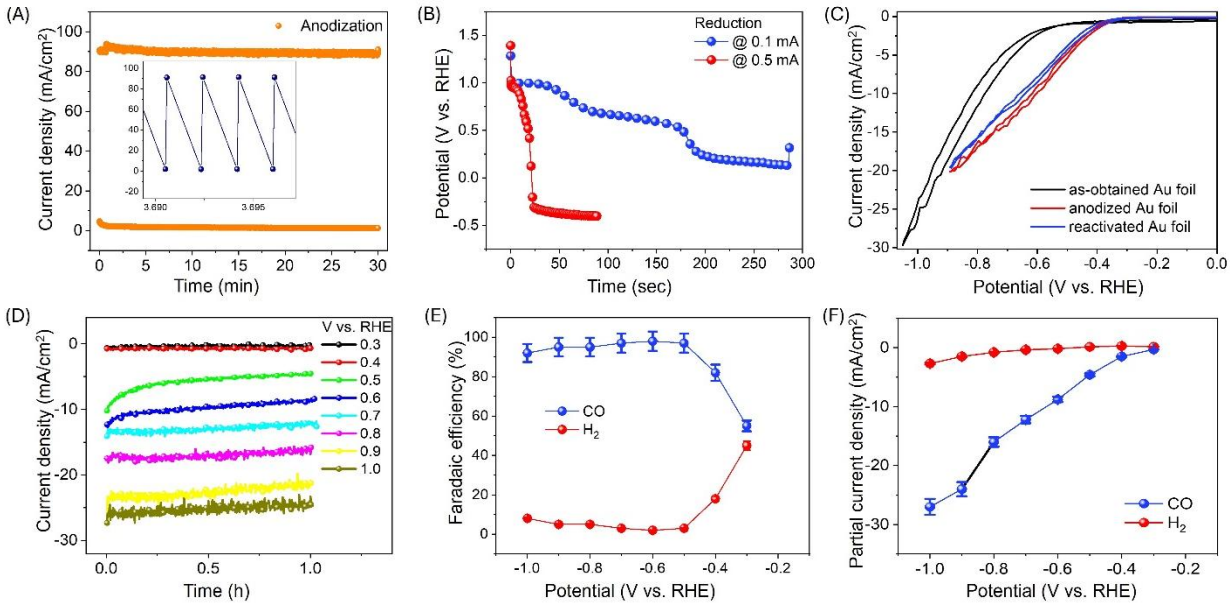


Figure 1 (a) Current density as a function of time for polycrystalline Au foil during pulsed anodization process for 30 min under 0.5 $KHCO_3$ electrolyte, (b) Electrochemical reduction on Ox-Au at different constant current densities, (c) Cyclic voltammetry (CV) curves of as obtained polycrystalline Au foil, anodized Au foil and Ox-Au (reactivated Au foil) under CO_2 saturated 0.5 $KHCO_3$ electrolyte at a scan rate of 20 mV/s, (d) Chronoamperometry curves at different applied potentials, (e) CO and H_2 faradaic efficiencies at different applied potentials and (f) CO and H_2 partial current densities at different applied potentials.

Before integrating the Ox-Au catalyst with the PEC system, the electrocatalytic CO_2 reduction performance was evaluated in an H-type electrochemical cell **(Figure S1)** under a CO_2-saturated 0.5 M $KHCO_3$ solution. After anodizing, the cyclic voltammetry (CV) profile of Ox-Au **(Figure 1c)** exhibits an apparent increase in total current density (j_{tot}) related to the CO_2 reduction reaction. Moreover, compared to the as-obtained Au-foil, the Ox-Au exhibits a positive shift in onset potential of ~0.2 V vs. RHE, revealing the importance of the anodization process. The shift in the onset potential of Ox-Au towards a positive direction is due to better CO_2 reduction in the presence of porous nanostructures, which not only enhance the CO_2 adsorption but also improve the CO_2 reduction reaction activity[36]. Next, the applied potentials-dependent selectivity of the Ox-Au catalyst was evaluated by chronoamperometry (CA), and the Faradaic efficiencies (FE) for CO and H_2 production were quantified by online gas chromatography. **Figures 1 (d, e)** show the CA curves and FEs at different applied potentials for the production of CO and H_2 using the Ox-Au in CO_2-saturated 0.5 M $KHCO_3$. The initial FE_{CO} is observed to be ~55% at an applied potential of –0.3 V vs. RHE. With increasing applied potentials, the production of CO and H_2 increases as consistent with the higher j_{tot} at higher applied potentials. A maximum FE_{CO} of ~98% is achieved at an overpotential of –0.5 V vs. RHE. Moreover, the FE of CO remains steady at >92% over a broad range of potentials from –0.6 V to –1.0 V vs. RHE. However, the FE_{CO} begins to drop at lower applied potentials, possibly due to changes in the local pH of the electrolyte.[29,35,37] The partial current density of CO_2RR (j_{co}) is shown in **Figure 1f,** which indicates that most of the j_{tot} is contributed to producing CO. Furthermore, the Ox-Au catalyst demonstrated stable FE_{CO} of ~90% at –1.0 V vs. RHE, maintaining 80% current density retention after 30 h of continuous operation, highlighting the excellent stability of the Ox-Au catalyst **(Figure S2)**. A plausible CO_2 reduction mechanism on the Ox-Au surface is

proposed and illustrated in **Figure S3**. Firstly, CO_2 is adsorbed onto the electron-rich porous Ox-Au surface, forming the *COO^- intermediate, which plays a crucial role in CO selectivity. The further addition and removal of electrons and protons in the *COO^- intermediate facilitates CO selectivity[38].

2. 2. Surface characterizations before and after CO_2RR.

After the anodization reaction followed by the reduction process, the X-ray diffraction pattern (XRD) indicates that the crystallinity of the Au remains unchanged **(Figure S4)**. This suggests that the anodization and reduction processes contribute to forming a porous nanostructure without affecting the crystal structure, which is beneficial for CO_2RR. Similar XRD results were reported in the literature for the Au film after the anodization process.[29] FE-SEM confirms the formation of porous nanostructures due to an anodization process **(Figure S5).** Transmission electron microscopy (TEM) was employed to probe the nanostructures of Ox-Au before and after CO_2RR. **Figure 2 (a, b)** depicts TEM images of the Au foil after the anodization process, revealing the formation of porous nanostructures on the surface. The high-resolution TEM image **(Figure 2c)** reveals the discontinuity of the crystal lattice fringes with the d-space value of 0.24 nm and grain boundaries with different orientations (marked in different colors).[39,40] The Fourier transform (FFT) pattern **(Inset of Figure 1 b)** displays the ring patterns, indicating the formation of single Au crystallites consistent with XRD crystal planes.[41] Furthermore, a high-resolution TEM image was obtained for Ox-Au after 25 h of continuous PEC CO_2RR, showing no signs of etching or corrosion even after prolonged operation **(Figure 2d and inset)**. The visible grain boundaries and sub-grains indicate that the anodized Au nanostructures remain stable during extended CO_2RR.

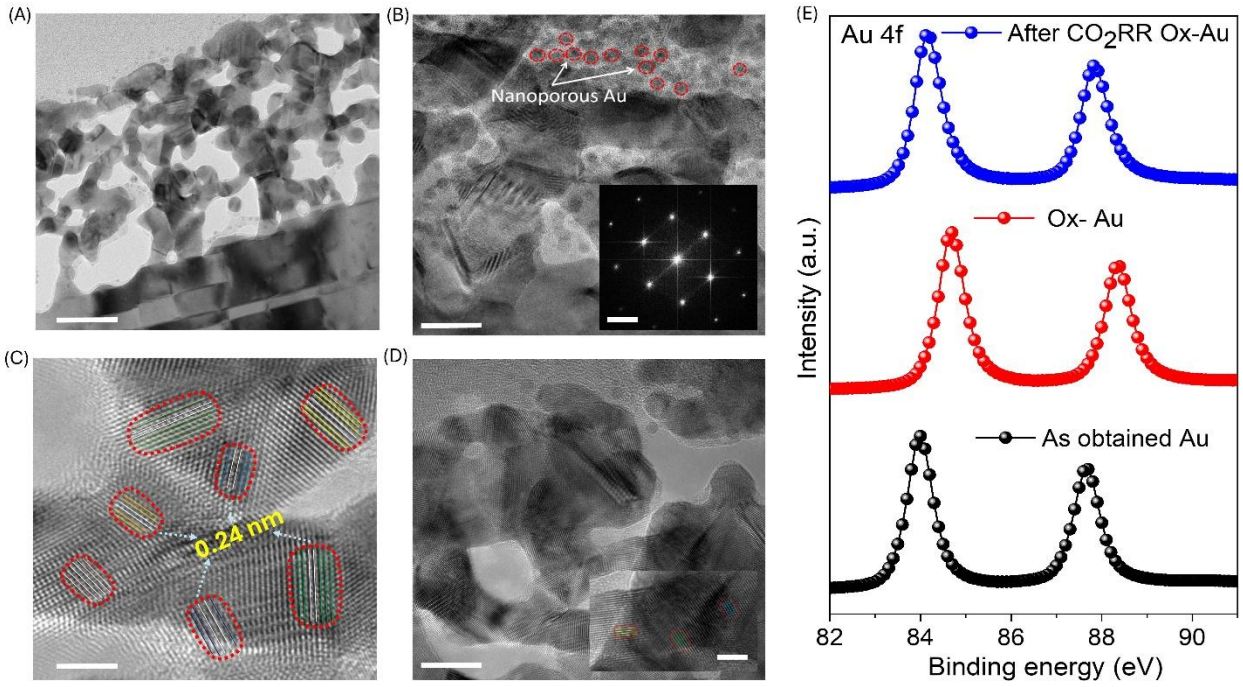


Figure 2 (a) shows the low-resolution TEM image of Ox-Au nanostructures before CO_2RR (scale bar – 50 nm). The top layer of the Au-foil has been anodized and converted into porous nanostructures. **Figures (b)** show the high-resolution TEM images of the nanostructures that reveal the different grain boundaries and sub-grains obtained from the pulsed anodization and reduction process. (scale bar–5 nm). The Inset of **Figure (b)** shows the ring Fourier transform (FFT) pattern, demonstrating the formation of single Au crystallites. **Figure (c)** shows the high-resolution TEM image of Ox-Au nanostructures with crystal lattice fringes in different orientations (scale bar – 2 nm). **Figure (d)** shows the high-resolution TEM image of Ox-Au nanostructures after 25 h of continuous CO_2RR (scale bar – 10 nm). The Inset of **Figure (d)** shows crystal lattice fringes in different orientations (scale bar – 2 nm). **Figure (e)** shows the high-resolution Au 4f XPS spectra of as-obtained Au-foil, Ox-Au, and after CO_2RR.

X-ray photoelectron spectroscopy (XPS) was utilized to examine changes in the oxidation states of an Au foil before and after pulsed anodization, followed by a reduction reaction. **Figure S6** shows the survey scan XPS spectra of Ox-Au before and after the PEC CO_2RR for 25 h, indicating the presence of Ox-Au after anodization and subsequent reduction. **Figure 2e** displays

the high-resolution Au 4f XPS spectra of the bare Au foil, after the anodization process, and after PEC CO_2RR. The high-resolution Au 4f XPS spectra of bare Au foil exhibit peaks at 84.0, and 88.2 eV corresponds to Au $4f_{7/2}$ and Au $4f_{5/2}$, indicating that Au is in a metallic state[36,37]. After the pulsed anodization step, the Au $4f_{7/2}$ peaks are shifted to the high binding energies side, suggesting electron depletion in the Au foil after the oxidation reaction. This electron deficiency is crucial for adsorbing CO_2 reduction intermediates on the catalyst surface.[42] As Ox-Au is electron-deficient, it can efficiently adsorb and stabilize $CO_2^{\bullet-}$ intermediates compared to the bare Au foil, creating favorable conditions for the CO_2 reduction reaction.[29] The LSV results **(Figure 1C)** well support this, showing that Ox-Au has a higher current density at a lower onset potential than the bare Au foil. However, the Au surface is mostly reduced to Au^0 after 25 h of PEC CO_2RR, where the Au $4f_{7/2}$ peak is shifted back to 84.2 eV but not to the original position of 84.0 eV.[37,43] These results confirmed that a thin layer of anodized Au is formed on the surface of Au foil during the pretreatment, which is reduced to Au^0 during the CO_2RR.

2. 3. Photoabsorber Design

It is important to have a photoabsorber with sufficient photovoltage to achieve high efficiency in standalone solar-driven fuel production reactions. When designing a photoabsorber, it is crucial to consider several factors. This includes the overpotentials of the CO_2RR-cathode catalyst and the oxygen evolution reaction (OER)-anode catalyst, as well as the overall system resistance (iR), and the thermodynamic potential required to reduce CO_2 into CO. Here, we employed the InGaP/GaAs/Ge (TJ) cell as a photoanode to drive unassisted PEC CO_2RR to CO production with high current densities. The structure of the TJ cell is illustrated in **Figure 3a**, and detailed fabrication information is available in the supporting information.[44] To study the structure and composition of the TJ cell photoabsorber, we conducted TEM and high-angle annular dark-field

scanning transmission electron microscopy (HAADF-STEM) along with cross-sectional elemental mapping **(Figure 3 b and c)**. The results demonstrate a tandem arrangement of the top GaInP cell, middle GaAs sub-cell, and bottom Ge sub-cell, respectively[45]. Further, the photovoltaic characteristics of TJ cell under AM 1.5G simulated sunlight illumination is shown in **Figure 3d.** Under AM 1.5G simulated sunlight, the TJ cell demonstrates a short-circuit current density (Jsc) of 13.5 mA/cm², an open-circuit voltage (Voc) of 2.5 V, and a fill factor (FF) of 0.83. Importantly, in tandem cells, the photovoltages of the sub-cells are additive. Consequently, the Voc achieved with the TJ cell exceeds the potential required to drive unassisted CO_2 reduction (~2.3 V). To study the light absorption properties of TJ cells, we have performed the external quantum efficiency measurement (EQE) with the absorption edge of each sub-cell. As shown in **Figure 3e**, the top GaInP cell with a band gap of 1.85 eV harvests photons in the 300 to 600 nm range. The middle GaAs sub-cell with a band gap of 1.40 eV facilitates photon absorption in the 600-900 nm range. Finally, the bottom Ge sub-cell with a band gap of 0.67 eV absorbs the photons ranging between 900 to 1800 nm. The EQE and Jsc studies of TJ cell reveal the efficient light absorption capability and charge carrier separation properties. Furthermore, to protect and drive the unassisted PEC CO_2RR in the aqueous electrolyte, RuOx-deposited Ti-foil was integrated on the back side of the TJ photoabsorber for OER at low onset potential.

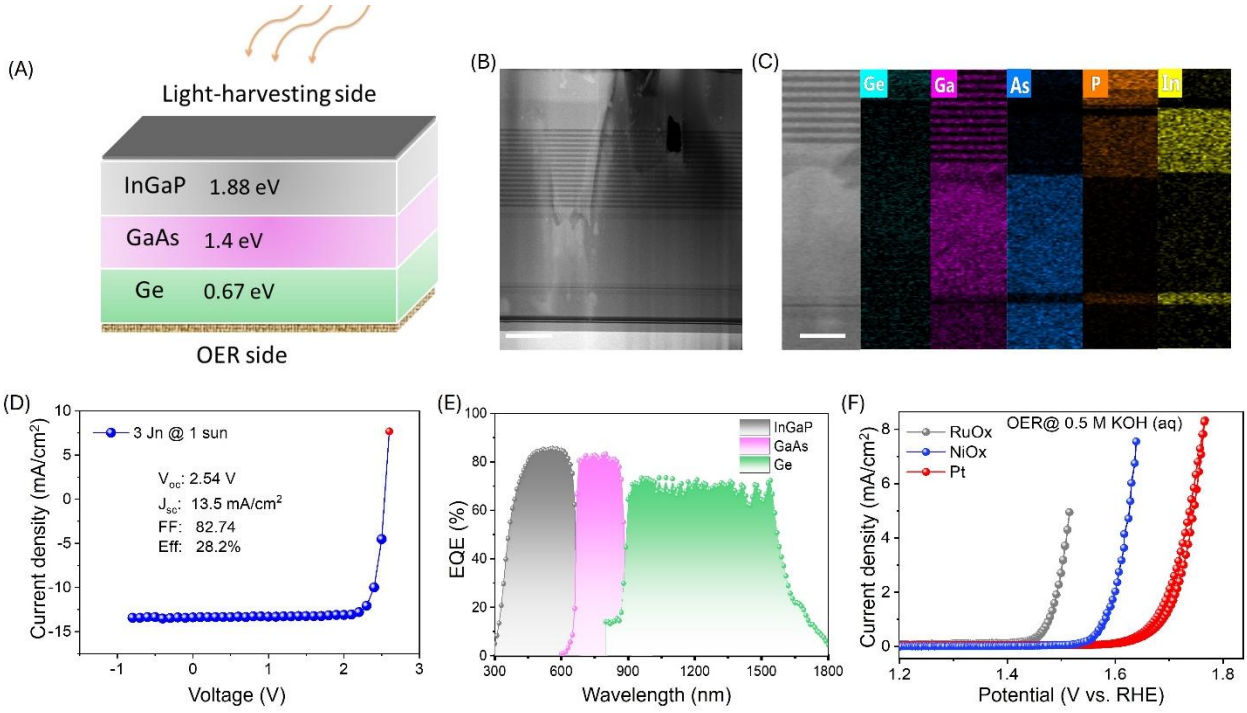


Figure 3 (a) Schematic architecture of Ge/InGaAs/InGaP triple junction (TJ) solar cell. **Figure (b)** Low-resolution transmission electron microscopy (TEM) image of the 3J InGaP/GaAs/Ge cell ((scale bar – 2μm). **Figure (c)** High-angle annular dark field scanning transmission electron microscopy images (HAADF–STEM) and elemental mapping images. **Figure (d)** J-V characteristics of the Ge/InGaAs/InGaP TJ photoabsorber under 1 sun AM 1.5G irradiation. **Figure (e)** External quantum efficiency studies of the Ge/InGaAs/InGaP TJ photoabsorber. **Figure (f)** OER performance of RuOx, NiOx and Pt in 0.5 M KOH electrolyte with a scan rate of 20mV/sec.

2. 4. Cell configuration and unassisted PEC CO_2RR

To achieve an efficient PEC CO_2RR approach, parameters such as OER catalysts, membranes, and electrolytes must be optimized before CO_2RR. This is due to several challenges, including the low solubility of CO_2 in alkaline environments and the competitive hydrogen production in acidic environments, which can impede the PEC CO_2RR performance.[16,27,45–51] The common OER electrocatalysts, such as Ni, Fe, and Co, can be used. However, obtaining the required potential for unassisted PEC is difficult because these catalysts can show high onset

potentials for OER.[27] As a result, to date, precious metal OER catalysts such as Pt and IrO_2 have been typically used to carry out coupled electrochemical water oxidation due to their stability in a neutral environment.[33] Even though using such precious metals for OER, the combination of reduction and oxidation still requires a total bias of at least ~3 V to produce a selective product at a significant yield (>10 mA cm^{-2}).[52] To match the independently optimized CO_2RR and OER catalysts and to eliminate any contamination, a BPM membrane is used.[8,33,53] BPM can provide favorable pH conditions for alkaline OER (KOH) and neutral CO_2RR ($KHCO_3$), leading to a significant reduction in the potential to drive CO_2RR. A tri-potentiostat study was conducted to optimize the BPM potential for the unassisted PEC CO_2RR reaction under different anolyte and catholyte pH conditions **(Figure S7)**. When selecting highly acidic and alkaline pH conditions for the anolyte and catholyte, respectively, such as 1 M KOH and 1 M H_2SO_4, the membrane potential was determined to be >0.7 V. However, these conditions are not suitable for cathodic CO_2 reduction since acidic electrolytes can promote the HER. Whereas the BPM exhibits a low membrane potential of <0.4 V in near-neutral pH conditions on the anode and cathode sides but OER rate can be sluggish in such conditions. Nevertheless, maintaining a near-neutral (0.5 M $KHCO_3$) and alkaline (1 M KOH) pH at the cathode and anode sides shows a favorable membrane potential than extremely highly acidic and alkaline conditions, which could favor CO_2 reduction. Finally, we analyzed the electrocatalytic overpotentials for the OER catalyst using RuOx, NiOx, and Pt catalysts at 1 M KOH (aq) to construct the unassisted PEC device. As shown in **Figure 3f,** the OER overpotentials of RuO_x, NiO_x, and Pt catalysts to reach 1mA/cm^2 are 300 mV, 410 mV, and 640 mV, respectively. These results show that RuO_x at 1M KOH combined with 0.5M $KHCO_3$ separated by BPM can drive the CO_2RR at ~2.3 V; hence, the TJ photoanode employment here is justified.

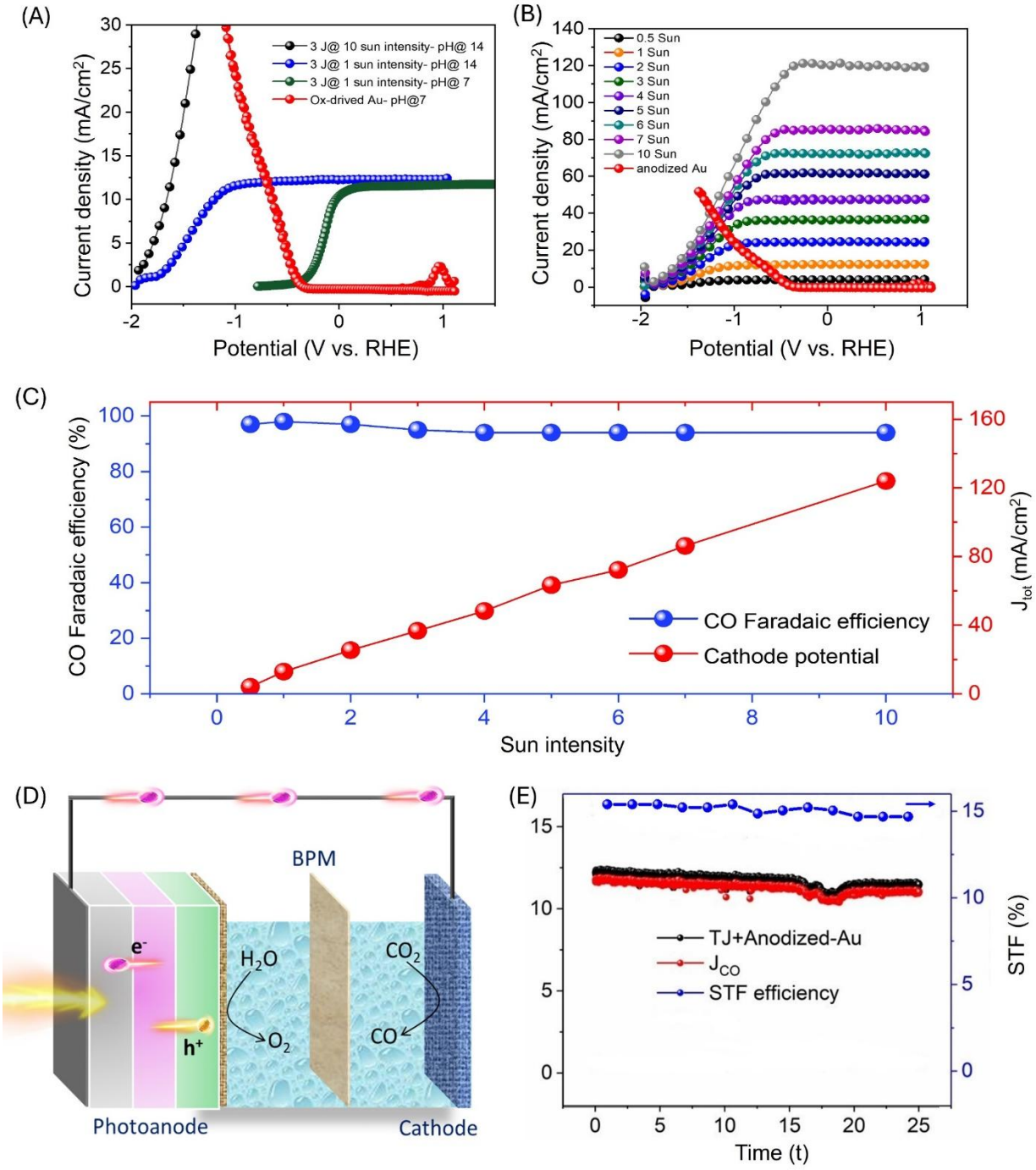


Figure 4 (a) shows the photoelectrochemical characteristics of TJ InGaP/GaAs/Ge photoanode measured at 1 sun intensity at pH 7 (green line), pH 14 (blue line), and at 10 sun intensity at pH 14 (grey line). The current density matches the cathodic characteristics of Ox-Au nanostructures measured under 0.5M $KHCO_3$ with CO_2 saturation. **Figure (b)** shows the behavior of TJ InGaP/GaAs/Ge photoanode under varying sun

intensity (up to 10 suns) and its total current densities the matching cathodic characteristics of Ox-Au. **Figure (c)** shows the total current densities and corresponding FE_{CO} by varying sun intensity. **Figure (d)** Schematic illustration of the unassisted device configuration for CO_2 to CO conversion. Unassisted two-electrode solar-driven CO_2RR by short-circuiting the TJ InGaP/GaAs/Ge photoanode with the dark cathode (Ox-Au). **Figure (e)** the total current density (J_{tot}), partial current density (J_{CO}), and STF conversion efficiency as a function of time.

Solar-driven CO_2RR was carried out in a customized H-cell reactor separated by a BPM membrane(**Figure S8)**.[33] The photoanode consists of a tandem-junction III–V photoabsorber (InGaP/GaAs/Ge/Ti/RuO_x), a thin Ti-foil (0.05 mm) surface protection layer, and a 25 nm of ALD deposited RuO_x to facilitate the OER, whereas the Ox-Au nanostructures were used as a dark cathode to drive the CO_2RR. Details of the fabrication of the photoanode and the reactor setup are described in the Supporting Information, and the fabricated photoanode image is shown in **Figure S9**. The oxidation behavior **(Figure 4a)** of the photoanode in 1 M KOH (aq) was investigated using CV without correcting for uncompensated resistance in a three-electrode electrochemical measurement setup under simulated one-sun illumination. The photoanode exhibited a light-limited photocurrent density of ~12.5 mA cm^{-2} and an equivalent open-circuit voltage of ~2.5 V in accordance with the photovoltaic characteristics of the TJ cell. The CV characteristics of the photoanode under pH 7 and the Ox-Au nanostructures are also shown in **Figure 4a.** The results show that in pH 7 the photovoltage delivered by the photoanode is insufficient to drive the unassisted CO_2RR as the current densities cross over at <1mA/cm^2. However, at pH 14, the photoanode delivers sufficient photovoltage for CO_2RR. This reveals the necessity of the BPM and the requirement of different catholytes and anolytes to drive the unassisted CO_2RR.

Further, it is essential to analyze the CO_2RR catalyst at commercially required current densities, to minimize the capital expenditure of a conversion unit to economically-compelling

levels. To achieve this, here we have done concentrated solar-driven CO_2RR in which the InGaP/GaAs/Ge/Ti/RuO_x photoanode is capable of working under >100 suns concentrated illumination. However, due to the PEC H-cell reactor's limitations and the diffusion limit of CO_2 in the electrolyte, we carried out the reaction at 10 sun intensity. Under concentrated 10 suns illumination, the oxidation behavior of the photoanode in 1 M KOH (aq) has been characterized by the CV in a three-electrode electrochemical measurement setup **(Figure 4b).** Here, three-electrode measurements are used due to the higher overpotential of RuO_x catalyst at higher J_{tot} compared to the one-sun illumination. Subsequently, chronoamperometry study was carried out for concentrated sunlight experiments at the potential of 0 V vs. RHE in a typical H-cell, and the photoanode exhibited a light-limited photocurrent density of ~124.8 mA cm^{-2}. In addition to this, the J_{tot} was stable over 25 h; however, the FE_{CO} reduced over time and reached as low as 60% within 1 hour with simultaneous enhancement in the FE_{H2} **(Figures S10 and S11)**. The reduced FE_{CO} can be explained by kinetic limitations of CO_2 saturation in a typical H-cell reactor with higher current densities.

Figure 4(c) shows the sun intensity-dependent total current densities and FE_{CO} (from 0.5 suns to 10 suns). Increasing sun intensity increases the total current densities of the InGaP/GaAs/Ge/Ti/RuO_x photoanode. The NMR analysis ensures no liquid product is formed during CO_2RR **(Figure S12)**. Unassisted two-electrode CO_2RR was also performed in the H-cell reactor by short-circuiting the InGaP/GaAs/Ge/Ti/RuO_x photoanode (0.8 cm^2) and ~1 cm^2 of Ox-Au catalyst as a counter electrode **(Figure 4d)**. CV with the two-electrode setup showed a short-circuit current density of ~11.5 mA cm^{-2}, which is ~1 mA cm^{-2} lower than the three-electrode setup, demonstrating the unassisted CO_2RR. This two-electrode measurement was utilized to calculate STF efficiency.[33] Corresponding to a current density of ~11.5 mA cm^{-2}, a maximum STF

of ~15% was achieved, considering the FE_{CO} of ~98%. In addition, we conducted a 25 h stability test in a two-electrode configuration to validate the claimed efficiency **(Figure 4e)**. Over the entire measurement period of ~25 hours, the J_{tot} was stable, and the FE_{CO} was ~96%. This results in the STF efficiency of ~15 % over the entire period. It is worth mentioning that the achieved PEC performance of the present system outperforms many reported literature **(Table 1).** Furthermore, following the stability experiment, we conducted XRD and SEM studies on the cathode Ox-Au, which revealed no significant changes during stability studies **(Figure S13)**.

3. Conclusions

In summary, we report an efficient and stable solar-driven CO_2RR system by integrating the Ox-Au as a cathode catalyst with the InGaP/GaAs/Ge/Ti/RuO_x photoanode that can drive the spontaneous CO_2RR. A bipolar membrane was employed to allow different pH electrolytes for the catholyte and anolyte, reducing the required overpotentials to drive the unassisted reaction. Under simulated AM 1.5G one-sun illumination, the reactor yields an operating j_{tot} of 11.5 mA cm^{-2}, indicative of the STF efficiency of ~15%. InGaP/GaAs/Ge/Ti/RuO_x system also allows one to use concentrated sunlight-driven CO_2 reduction up to ten sun intensity, in which the efficiency scales up linearly with reduced FE for CO due to the diffusion limits of the H-cell reactor.

CARBON ENERGY Open Access

WILEY

Supporting Information

Supporting Information is available from the Wiley Online Library or from the author.

Acknowledgments

This work is supported by the City University of Hong Kong (9380107 and 7005943), King Abdullah University of Science and Technology, and Agency for Science, Technology and Research (C230415018 and C231218003). K.P., V.R., and P. V. contributed equally to this work.

Conflict of Interest

The authors declare no conflict of interest

References

1. Zhu P, Wang H. High-purity and high-concentration liquid fuels through CO_2 electroreduction. *Nat. Catal. 2021;* 4(11):943-951.

2. What Else Can Photoelectrochemical Solar Energy Conversion Do Besides Water Splitting and CO_2 Reduction? *ACS Energy Lett.* 2018*;* 3 (10): 2610–2612.

3. Montoya JH, Seitz LC, Chakthranont P, Vojvodic A, Jaramillo TF, Nørskov JK. Materials for solar fuels and chemicals. *Nat. Mater.* 2016;16(1):70-81.

4. Hiragond CB, Biswas S, Powar NS, et al. Surface-modified Ag@Ru-P25 for photocatalytic CO_2 conversion with high selectivity over CH_4 formation at the solid–gas interface. *Carbon Energy*. 2024;6:e386.

5. Gong E, Ali S, Hiragond CB, et al. Solar fuels: research and development strategies to accelerate photocatalytic CO_2 conversion into hydrocarbon fuels. *Energy Environ Sci*. 2021;15(3):880-937.

6. Kumaravel V, Bartlett J, Pillai SC. Photoelectrochemical Conversion of Carbon Dioxide (CO_2) into Fuels and Value-Added Products. *ACS Energy Lett.* 2020; 5(2): 486–519.

7. Liu B, Wang T, Wang S, et al. Back-illuminated photoelectrochemical flow cell for efficient CO_2 reduction. *Nat. Commun.* 2022;13(1):1-8.

8. Urbain F, Tang P, Carretero NM, et al. A prototype reactor for highly selective solar-driven CO_2 reduction to synthesis gas using nanosized earth-abundant catalysts and silicon photovoltaics. *Energy Environ Sci*. 2017;10(10):2256-2266.

9. Ramalingam V, Varadhan P, Fu HCCH c, et al. Heteroatom-Mediated Interactions between Ruthenium Single Atoms and an MXene Support for Efficient Hydrogen Evolution. *Adv. Mater.* 2019;31(48):1-10.

10. Wang L, Cheng H, Zhang Z, et al. Rational design of honeycomb-like APTES-TiO_2/COF heterostructures: Promoted intramolecular charge transfer for visible-light-driven catalytic CO_2 reduction. *Chem. Eng. J*. 2023;456:140990.

11. Hou H, Shao G, Wang Y, Wong WY, Yang W. Insights on advanced substrates for controllable fabrication of photoanodes toward efficient and stable photoelectrochemical water splitting. *Carbon Energy*. 2024;6(4):e373.

12. Song K, Hou H, Zhang D, He F, Yang W. In-situ cation-exchange strategy for engineering single-atomic Co on TiO_2 photoanode toward efficient and durable solar water splitting. *Appl*. *Catal B*. 2023;330:122630.

13. Song K, Hou H, Gong C, et al. Enhanced solar water splitting of $BiVO_4$ photoanodes by in

situ surface band edge modulation. *J Mater Chem A* 2022;10(42):22561-22570.

14. Jouny M, Luc W, Jiao F. General Techno-Economic Analysis of CO_2 Electrolysis Systems. *Ind Eng Chem Res*. 2018;57(6):2165-2177.

15. Ethylene Electrosynthesis: A Comparative Techno-economic Analysis of Alkaline vs Membrane Electrode Assembly vs CO_2 −CO− C_2 H_4 Tandems. *ACS Energy Lett.* 2021; 6(3): 997 1002.

16. Dinh CT, García De Arquer FP, Sinton D, Sargent EH. High rate, selective, and stable electroreduction of CO_2 to co in basic and neutral media. *ACS Energy Lett*. 2018;3(11):2835-2840.

17. Hernández S, Farkhondehfal MA, Sastre F, Makkee M, Saracco G, Russo N. Syngas production from electrochemical reduction of CO_2: current status and prospective implementation. *Green Chemistry*. 2017;19(10):2326-2346.

18. Wang L, Huang G, Zhang L, et al. Construction of TiO_2-covalent organic framework Z-Scheme hybrid through coordination bond for photocatalytic CO_2 conversion. *J. Ener. Chem*. 2022;64:85-92.

19. Kistler TA, Um MY, Cooper JK, Sharp ID, Agbo P. Monolithic Photoelectrochemical CO_2 Reduction Producing Syngas at 10% Efficiency. *Adv. Energy Mater*. 2021;11(21):2100070.

20. Li A, Wang T, Chang X, et al. Tunable syngas production from photocatalytic CO_2 reduction with mitigated charge recombination driven by spatially separated cocatalysts. *Chem Sci*. 2018;9(24):5334-5340.

21. Ma M, Hansen HA, Valenti M, et al. Electrochemical reduction of CO_2 on compositionally variant Au-Pt bimetallic thin films. *Nano Energy*. 2017;42:51-57.

22. Chang X, Wang T, Yang P, et al. The Development of Cocatalysts for Photoelectrochemical CO_2 Reduction. *Adv. Mater*. 2019;31(31):1804710.

23. Dong WJ, Navid IA, Xiao Y, et al. Bi catalysts supported on GaN nanowires toward efficient photoelectrochemical CO_2 reduction. *J. Mater. Chem. A*. 2022;10(14):7869-7877.

24. Raciti D, Wang C. Recent Advances in CO_2 Reduction Electrocatalysis on Copper. *ACS Energy Lett*. 2018;3(7):1545-1556.

25. Li P, Yang F, Li J, et al. Nanoscale Engineering of P-Block Metal-Based Catalysts Toward Industrial-Scale Electrochemical Reduction of CO_2. *Adv. Energy Mater*. 2023;13(34):2301597.

26. Fan L, Xia C, Yang F, Wang J, Wang H, Lu Y. Strategies in catalysts and electrolyzer design for electrochemical CO_2 reduction toward C_{2+} products. *Sci Adv*. 2020;6(8):1-18.

27. Lu Q, Jiao F. Electrochemical CO_2 reduction: Electrocatalyst, reaction mechanism, and process engineering. *Nano Energy*. 2016;29:439-456.

28. Mariano RG, McKelvey K, White HS, Kanan MW. Selective increase in CO_2 electroreduction activity at grain-boundary surface terminations. *Science*. 2017;358(6367):1187-1192.

29. Chen Y, Li CW, Kanan MW. Aqueous CO_2 reduction at very low overpotential on oxide-derived au nanoparticles. *J Am Chem Soc*. 2012;134(49):19969-19972.

30. Li D, Yang K, Lian J, Yan J, Liu S. Powering the World with Solar Fuels from Photoelectrochemical CO_2 Reduction: Basic Principles and Recent Advances. *Adv. Energy Mater*. 2022;12(31):2201070.

31. Wang Y, Liu J, Wang Y, Wang Y, Zheng G. Efficient solar-driven electrocatalytic CO_2 reduction in a redox-medium-assisted system. *Na. Commun.* 2018;9(1):1-8.

32. Zhang Z, Chi M, Veith GM, et al. Rational Design of Bi Nanoparticles for Efficient Electrochemical CO_2 Reduction: The Elucidation of Size and Surface Condition Effects. *ACS Catal*. 2016;6(9):6255-6264.

33. Zhou X, Liu R, Sun K, et al. Solar-Driven Reduction of 1 atm of CO_2 to Formate at 10% Energy-Conversion Efficiency by Use of a TiO_2-Protected III-V Tandem Photoanode in Conjunction with a Bipolar Membrane and a Pd/C Cathode. *ACS Energy Lett*. 2016;1(4):764-770.

34. Khan B, Faheem MB, Peramaiah K, et al. Unassisted photoelectrochemical CO_2-to-liquid fuel splitting over 12% solar conversion efficiency. *Nat. Commun.* 2024;15(1):1-13.

35. Feng X, Jiang K, Fan S, Kanan MW. Grain-Boundary-Dependent CO_2 Electroreduction Activity. *J Am Chem Soc*. 2015;137(14):4606-4609.

36. Song JT, Ryoo H, Cho M, et al. Nanoporous Au Thin Films on Si Photoelectrodes for Selective and Efficient Photoelectrochemical CO_2 Reduction. *Adv Energy Mater*. 2017;7(3):1601103.

37. Feng X, Jiang K, Fan S, Kanan MW. A direct grain-boundary-activity correlation for CO electroreduction on Cu nanoparticles. *ACS Cent Sci*. 2016;2(3):169-174.

38. Chen S, Chen A. Electrochemical Reduction of Carbon Dioxide on Au Nanoparticles: An in Situ FTIR Study. *J. Phys. Chem. C*. 2019; 123 (39): 23898–23906.

39. Kim J, Song JT, Ryoo H, Kim JG, Chung SY, Oh J. Morphology-controlled Au nanostructures for efficient and selective electrochemical CO_2 reduction. *J. Mater. Chem. A*. 2018;6(12):5119 5128.

40. Jin Y, Hwang J, Han MK, Shon W, Rhyee JS, Kim SJ. Size-Controlled Au-Cu_2Se Core-Shell Nanoparticles and Their Thermoelectric Properties. *ACS Appl. Mater. Interfaces*. 2020;12(32):36589-36599.

41. Li J, Liu CY, Liu Y. Au/graphene hydrogel: synthesis, characterization and its use for catalytic reduction of 4-nitrophenol. *J. Mater. Chem*. 2012; 22(17): 8426-8430.

42. Kim Y, Kim B, Choi H, Kim S, Yun Y, Oh J. Modulating the electronic structure of Au using a heterostructure for efficient electrochemical CO_2 reduction. *Chem. Eng. J*. 2023;461:142126.

43. Peramaiah K, Ramalingam V, Fu HC, et al. Optically and Electrocatalytically Decoupled Si Photocathodes with a Porous Carbon Nitride Catalyst for Nitrogen Reduction with Over 61.8% Faradaic Efficiency. *Adv. Mater*. 2021;33(18):2100812.

44. Li W, Fu HC, Zhao Y, He JH, Jin S. 14.1% Efficient Monolithically Integrated Solar Flow Battery. *Chem*. 2018;4(11):2644-2657.

45. Chen C, Khosrowabadi Kotyk JF, Sheehan SW. Progress toward Commercial Application of Electrochemical Carbon Dioxide Reduction. *Chem*. 2018;4(11):2571-2586.

46. Huang H, Periyanagounder D, Chen C, et al. Artificial Leaf for Solar-Driven Ammonia Conversion at Milligram-Scale Using Triple Junction III-V Photoelectrode. *Adv. Sci*. 2023:10(14): 2205808.

47. Pătru A, Binninger T, Pribyl B, Schmidt TJ. Design Principles of Bipolar Electrochemical Co-Electrolysis Cells for Efficient Reduction of Carbon Dioxide from Gas Phase at Low Temperature. *J Electrochem Soc*. 2019;166(2):F34-F43.

48. Vermaas DA, Wiegm.an S, Nagaki T, Smith WA. Ion transport mechanisms in bipolar membranes for (photo)electrochemical water splitting. *Sustain. Ener. Fuels.* 2018; 2(9): 2006-2015.

49. Yan Z, Zhu L, Li YC, et al. The balance of electric field and interfacial catalysis in promoting water dissociation in bipolar membranes. *Energy Environ. Sci*. 2018;11(8):2235-2245.

50. Salvatore DA, Weekes DM, He J, et al. Electrolysis of Gaseous CO_2 to CO in a Flow Cell with a Bipolar Membrane. *ACS Energy Lett*. 2018;3(1):149-154.

51. Castro S, Albo J, Irabien A. Photoelectrochemical Reactors for CO_2 Utilization. *ACS Sustain Chem Eng*. 2018;6(12):15877-15894.

52. Vermaas DA, Smith WA. Synergistic Electrochemical CO_2 Reduction and Water Oxidation with a Bipolar Membrane. *ACS Energy Lett*. 2016;1(6):1143-1148.

53. Vargas-Barbosa NM, Geise GM, Hickner MA, Mallouk TE. Assessing the Utility of Bipolar Membranes for use in Photoelectrochemical Water-Splitting Cells. *ChemSusChem*. 2014;7(11):3017-3020.